METRICA
METRology Institutional CAtalog

ISTITUTO NAZIONALE DI RICERCA METROLOGICA
Repository Istituzionale

Magnetization switching in high-density magnetic nanodots by a fine-tune sputtering process on a large-area diblock copolymer mask

This is the author's submitted version of the contribution published as:

Original
Magnetization switching in high-density magnetic nanodots by a fine-tune sputtering process on a large-area diblock copolymer mask / Barrera, Gabriele; Celegato, F; Coïsson, M; Manzin, A; Ferrarese Lupi, F; Seguini, G; Boarino, L; Aprile, G; Perego, M; Tiberto, P. - In: NANOSCALE. - ISSN 2040-3372. - 9:43(2017), p. 16981-16992. [10.1039/c7nr04295g]

Availability:
This version is available at: 11696/56923 since: 2018-01-30T10:37:52Z

Publisher:
RSC Publishing

Published
DOI:10.1039/c7nr04295g

Terms of use:

This article is made available under terms and conditions as specified in the corresponding bibliographic description in the repository

Publisher copyright

(Article begins on next page)

30 June 2024

Magnetization switching in high-density magnetic nanodots by a fine-tune sputtering process on large area diblock copolymer mask

Gabriele Barrera,[†] Federica Celegato, [†] Marco Coïsson,[†] Alessandra Manzin,[*] Federico Ferrarese Lupi, [†,§] Gabriele Seguini, [§] Luca Boarino, [†] Giulia Aprile, [†,‡] Michele Perego[§] and Paola Tiberto, [†]

[†]INRiM, Divisione Nanoscienze e materiali, Strada delle Cacce 91, 10135 Torino, Italy,

[*]INRiM, Divisione Metrologia per la qualità della vita, Strada delle Cacce 91, 10135 Torino, Italy,

[§]Laboratorio MDM, IMM_CNR, Via C. Olivetti 2, 20864 Agrate Brianza (MB), Italy,

[‡]Dipartimento di scienze innovazione tecnologica (DIST), Università del Piemonte Orientale "A. Avogadro", INSTM, UdR Alessandria, Viale T. Michel 11, 1512 Alessandria, Italy.

KEYWORDS Diblock copolymer, magnetic Nanodot arrays, Spuettering process

ABSTRACT

Ordered magnetic nanodot arrays with extremely high density provide unique properties to the always/still growing field of nanotechnology. To overcome size limits of conventional lithography, a fine-tuned sputtering process on diblock-copolymer templates is here proposed to fabricate uniform and densely spaced nanometer-scale magnetic nanodots arrays. This process has been successfully exploited to pattern, over a large area, sputtered $Ni_{80}Fe_{20}$ and Co thin films with thickness of 10 and 13 nm, respectively. A carefully tuned sputter-etching at a suitable glancing angle has been performed in order to selectively remove the magnetic material ending up with nanodot arrays (dot diameter of about 17 nm). A detailed study of magnetization reversal at room temperature as a function of sputter-etching time together with morphology investigations have been made to confirm the synthesis of long-range ordered arrays displaying functional magnetic properties. Hysteresis loops of the obtained nanodot arrays have been measured at different temperatures and interpreted by means of micromagnetic simulations to explore the role of dipole-dipole magnetostatic interactions between dots and the effect of magnetocrystalline anisotropy. The agreement between measurement and numerical modelling results addresses the use of the proposed synthesis technique as an innovative process to design large-area nanoscale arrays of functional magnetic elements.

In the last decade, magnetic nanostructures arranged in patterned arrays have attracted considerable interest in both fundament and applied research as they represent the key components of several magnetic devices and sensors. [Nalwa, Yang, Bai]

Various nanofabrication processes have been developed offering exceptional capabilities in structuring magnetic materials with fine control of shape, size, composition and density of nanostructures [Owens, Adeyeye, Tiberto]. This high degree of control is reflected in the possibility to easily tune the magnetic functional properties for a variety of applications (*e.g.* magnetic nanostructures for biomedical uses [Goiriena-Goikoetxea], magnetologic circuits [Gross], magnetic random access memories and hard disks [Yang, Ruiz]). In this framework, several conventional, sequential lithographic techniques (*e.g.* optical, electron beam, X-ray and nanoimprint lithographies) are extensively employed in both lift-off and etching based approaches [Olayo-Valles, Shin, Valbusa, Zhu, Ilievski]. However, the continuous quest for reducing the device dimensions at sub-20 nm level has almost led to reach the experimental limits making such methods more challenging and expensive [ITRS International Technology Roadmap for Semiconductors (ITRS), Emerging Research Materials 2011]. As a consequence, alternative processes have been recently proposed [Baruth, Kun-Hua Tu]. Among these, the block copolymer (BCP) nanolithography emerges as a rising powerful technique for fabrication of large-area polymeric templates structured on nanometer length scale that can be easily transferred to many different systems by means of a variety of processes[Kun-Hua Tu, Hawker, REF: Hamley2, Olayo-Valles, Jung, Tavakkoli, Suh].

Highly immiscible BCPs have the ability to self-assemble in a controlled way into highly periodic arrays with different morphology, such as lamellae, gyroids, spheres, and cylinders [Hawker, Hamely2, Hamely1, Perego]. The selective removal of the cylindrical block polymer

allows forming a highly-ordered template with holes, having characteristic dimensions as diameter and hole-to-hole distance that can be finely tailored by tuning the synthesis parameters [Ferrarese].

Magnetic nanodot arrays prepared by self-assembled BCP templates with holes can provide a novel class of systems to investigate the magnetic properties occurring at the nanoscale length [Ferré]. Unique magnetic phenomena not observed in bulk materials such as magnetic vortex state, skyrmion magnetization configuration, single domain behavior or superparamagnetic state can arise in confined magnetic ordered arrays. [Chun-Hao Lin, Skrm2,]. In addition, the flexibility of BCP templating technique allows to change inter-dot distance and thus tune the dipole-dipole magnetostatic interactions among nanodots, guaranteeing a greater control of the magnetization dynamics of the whole array [Cheng, Chen Xu, Cowburn].

In this work, a fine-tuned sputtering process on the self-assembling of cylinder-forming diblock copolymers (DBCs) has been exploited to produce through successive steps large-area arrays of Co and $Ni_{80}Fe_{20}$ nanodots with a diameter and center-to-center dot distance of about 17 nm and 35 nm, respectively. The magnetic materials are sputtered on DBC mask and subsequently a sputter etching at a suitable glancing angle is performed, in order to overcome the complexity of conventional lift-off process at the nanometer scale that can affect arrays final functional properties.

A detailed study of magnetization reversal is finalized to investigate the magnetic properties of the fabricated nanodots array. Micromagnetic simulations have been performed to interpret the experimental data and to get an insight on the impact of dipole-dipole magnetostatic interactions and magnetocrystalline anisotropy properties on the magnetic behavior of nanodot arrays.

RESULTS AND DISCUSSION

Nanofabrication process

The nanofabrication method here proposed can be divided in two main stages. The first one leads to the formation of a mask containing holes by DBC lithography on a SiO_x/Si substrate neutralized by an high temperature grafting of a P(S-*r*-MMA) random copolymer (RCP) [Ferrarese]. The second one concerns the deposition of the magnetic material layer (ML, Co or $Ni_{80}Fe_{20}$ in this paper) on the DBC mask and ends up with the formation of a magnetic nanodot array. The multi-steps process used to obtain the nanostructured system is schematically illustrated in Figure 1(a-d), where SEM images were taken in order to investigate the evolution of the sample morphology during the nanofabrication process. The SEM images reported in Figure 1(a-d) correspond to the Co sample and they are also representative for the morphology evolution of the $Ni_{80}Fe_{20}$ one. In the first step of nanofabrication process (Figure 1a), the DBC template is deposited on RCP-functionalized SiO_2 substrate as described in [Perego2, Ferrarese]. As shown in the corresponding SEM image, the resulting DBC template consists in a polystyrene (PS) matrix with well-ordered pores hexagonally arranged with quasi-homogeneous geometrical parameters (diameter $d \sim 17$ nm and center-to-center distance $L_0 \sim 35$ nm). The template thickness t is approximately 30 nm.

Subsequently, a magnetic thin film ($Ni_{80}Fe_{20}$ or Co) is deposited by rf-sputtering onto the obtained DBC template (Figure 1b). The magnetic material is deposited both in the pores and on top of PS matrix. The thickness of magnetic layer is about 10 nm and 13 nm for $Ni_{80}Fe_{20}$ and Co,

respectively. The corresponding SEM image shows how the deposited film follows the morphology of the underlying DBC template where the darker points correspond to the original holes of DBC in which now the magnetic material has been deposited. Since the sputtering is a conformal deposition technique, it is reasonable to assume that a very thin layer of deposited magnetic material covers also the vertical walls of cylindrical holes, forming a continuous thin film with a uneven surface; a representative sketch is proposed in Figure 1e.

Afterwards, in order to remove the unwanted magnetic material deposited on top of BCP template, a Ar^+ ions sputter etching at a glancing angle is performed (Figure 1c). The purpose of the glancing angle etching is to remove in a preferential and faster way the magnetic material on the top surface of DBC while leaving unaffected the magnetic material in the holes due to the shading effect guaranteed by the vertical cylinders of the DBC mask. The glancing angle, equal to 45° with respect to the normal to the sample plane, is chosen in accordance to the aspect-ratio of the DBC mask (Figure 1e)in order to not leave exposed to the etching ions the magnetic material deposited at the bottom of cylinders. The corresponding SEM image (Figure 1c) is taken just before the ending of the 45°-etching process and shows an initial appearance of magnetic nanodots array, but a small amount of residual magnetic material is clearly still present on top of DBC template. The main limitation of this 45°-etching process is that the magnetic material deposited on the vertical walls of the holes is also partially shaded (the right wall in Figure 1e) and therefore difficult to remove, unless a continuous rotation of the sample performed during this step. Although in our experimental set-up, the sample rotation cannot be implemented, the small amount of remaining magnetic material does not turn out to affect the magnetic properties of the resulting nanodots, as it will be discussed in the following.

In this process step, the 45°-sputter-etching time is finely tuned in order to completely remove the unwanted magnetic material deposited on top of DBC template in order to expose the PS matrix a second time; this makes easier the subsequent dissolution of the residual PS in toluene, ending up with the sole magnetic dots array on the substrate (Figure 1d). This procedure has been proven to be suitable to fabricate single-layer nanostructures and can be considered as a valid alternative to the common lift-off process that becomes progressively more difficult to be exploited in the limit of small features size, as already discussed by Baruth et al. [Baruth], who proposed the alternative non-lift-off Damascene-style patterning process to obtain an array of dots having a diameter of 25 nm.

After completion of the fabrication process, a well-ordered magnetic dot array is formed as represented by the SEM image (Figure 1d) revealing a local, hexagonal close-packed geometry with dot diameter ($d \sim 17$ nm) and center-to-center distance ($L_0 \sim 35$ nm). The resulting magnetic nanodots array perfectly mimic the pristine DBC template. The distribution of nanodot diameter of the Co sample, reported in Figure 1f, confirms the process reliability in successfully transferring the DBC pattern to the final magnetic dot array. The diameter distribution follows a Gaussian bell curve with mean diameter of 17.3 nm and standard deviation of 2.3 nm.

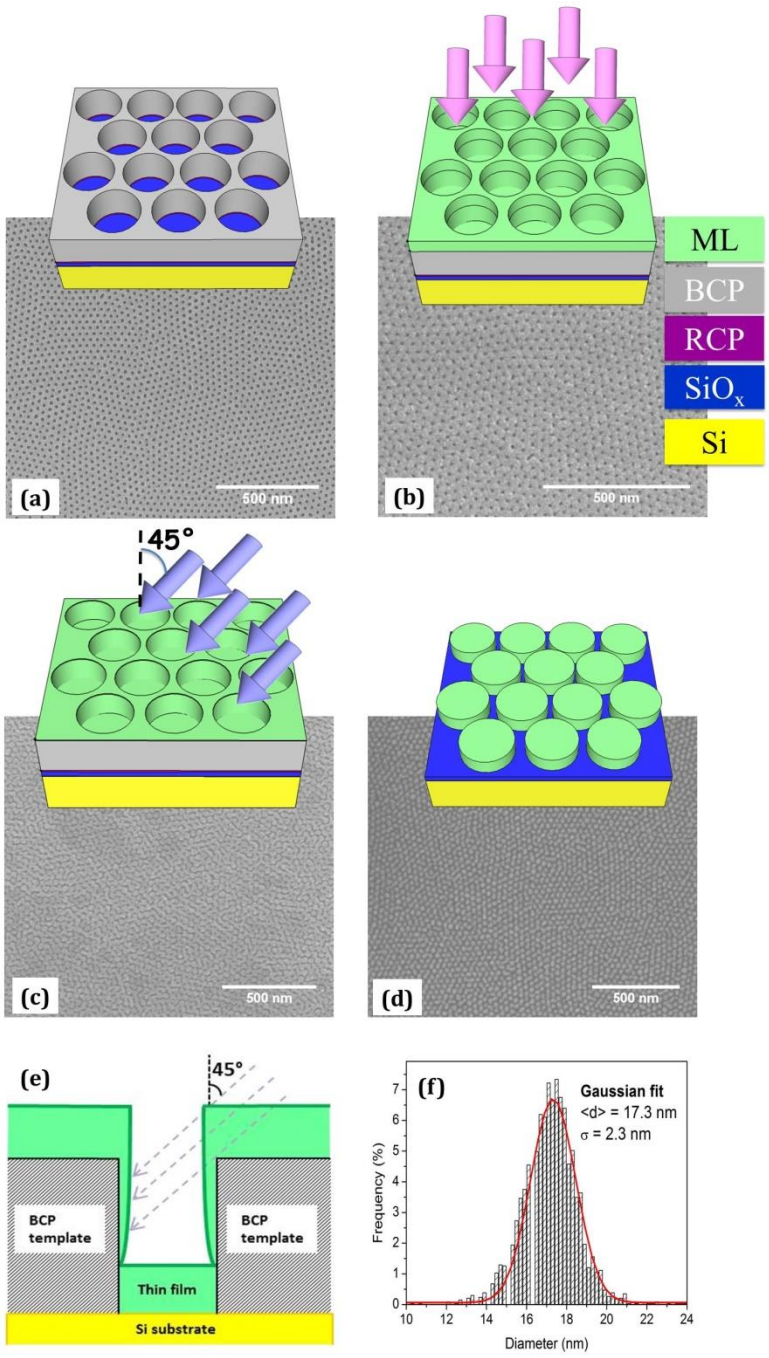

Figure 1. (a-d) schematic description of the nanofabrication process and corresponding SEM images related to Co sample: (a) synthesis of self-assembled DBC template; (b) deposition of magnetic thin film (ML) by rf-sputtering onto the BCP template; (c) Ar^+ sputter-etching

performed at an angle of 45° with respect to the normal to the sample plane; (d) final magnetic dot array; (e) in-scale sketch of 45° angle sputter etching; (f) nanodot diameter distribution derived from the analysis of SEM images after 150 s of sputter-etching.

Magnetic properties dependence on film morphology: influence of sputter etching time

Each step in the fabrication process strongly affects the functional properties of the final dot array. In particular, the time calibration of the 45°-sputter etching process is crucial to determine the final topology (as shown above) and the magnetic properties of the final magnetic nanostructure. In this context, the evolution of the magnetic properties as a function of the progressive formation of the magnetic nanostructure during the etching process can be followed by carefully tuning the sputter etching time (t_{etch}), starting from the as-deposited thin film on DBC template (t_{etch} = 0 s) and ending when completely isolated nanodots are obtained in an array (t_{etch} = 150 s). To this aim, the same sample is repeatedly measured after stopping the 45°-sputter etching at selected times (t_{etch} = 0 s, 60 s, 90 s, 120 s, 150 s).

The room-temperature hysteresis loops corresponding to the same Co sample etched for different, increasing t_{etch} are reported in Figure 2 together with the evolution of squareness ratio (M_R/M_S), saturation magnetization (M_S, values taken at 5 kOe where the curve is completely flat) and coercive field (H_C). This allows to single out the effect on magnetic properties of the progressive removal of the magnetic layer from the top of the DBC template, eventually revealing the magnetic behavior of isolated dot array. The diamagnetic contribution of the DBC mask, which has not yet been removed in this fabrication process step, has been conveniently subtracted before the magnetization curves are plotted in Figure 2.

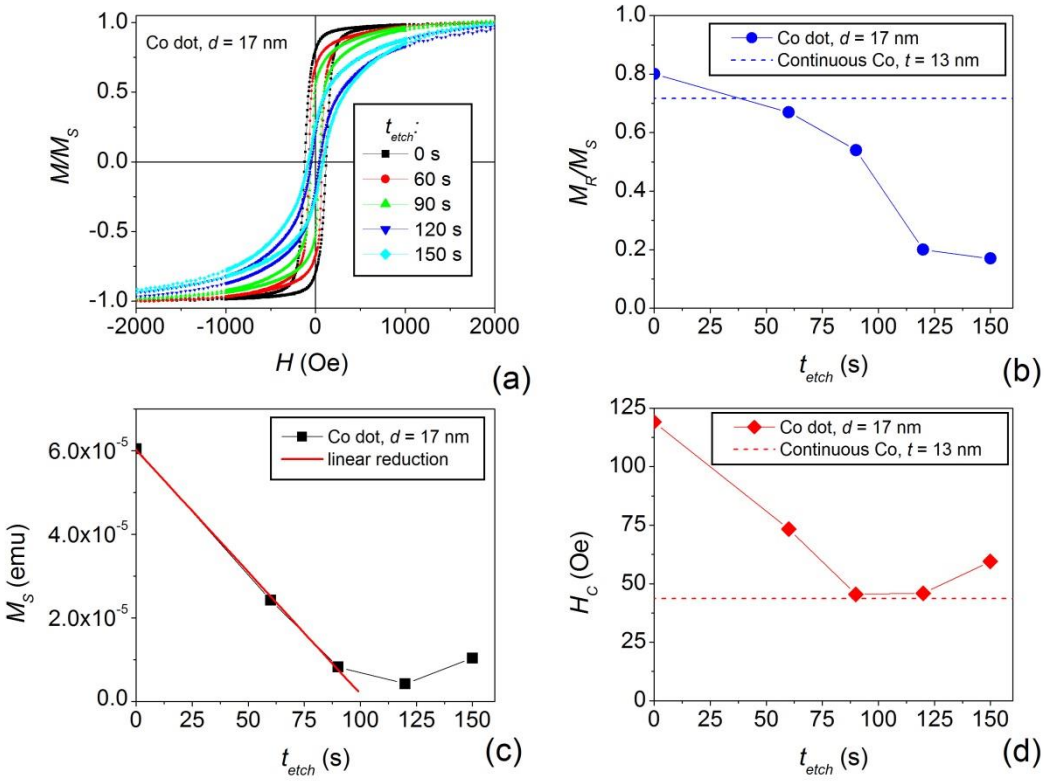

Figure 2. Evolution of magnetic properties as a function of sputter etching time: (a) room-temperature hysteresis loops; (b) hysteresis loop squareness (M_R/M_S); (c) saturation magnetization (M_S) and (d) coercive field (H_C). Dotted lines mark the values of the corresponding reference continuous Co thin film deposited on Si substrate. Continuous line in panel (c) shows the linear etching rate of the magnetic layer on top of the BCP matrix during the removal process.

The progressive removal of the Co top layer can be evidenced by the magnetization behavior extrapolated from the measured hysteresis loops shown in Figure 2a. It immediately emerges that the increasing in etching time leads to an ever slower approach to magnetic saturation. In

particular, the magnetization reversal of as-deposited thin film on the DBC mask (t_{etch} = 0 s, black curve in Figure 2a) shows a rather rectangular hysteresis loop, in which magnetization switching occurs in a narrow field interval (around H_C) with a well-defined and sharp magnetization jump. As a consequence, this loop has a high squareness value (M_R/M_S = 0.8) (Figure 2b), even higher than that of the reference continuous Co thin film deposited on a flat Si substrate (dotted line in Figure 2b). As t_{etch} increases, the field interval in which the magnetization reverses gradually becomes wider with a correspondingly less sharp magnetization jump. In this case, the value of hysteresis loop squareness monotonically reduces to M_R/M_S = 0.17 at t_{etch} = 150 s (Figure 2b). Such a change marks the onset of a different magnetization regime strongly influenced by the presence of magnetic islands becoming more and more isolated with increasing etching times.

The effect of the progressive removal of the Co top layer is also evidenced by the corresponding monotonous decrease in M_S with increasing t_{etch} reported in Figure 2c. In particular, it is notable a linear reduction in M_S up to t_{etch} = 90 s indicating a linear etching rate of the magnetic material on top of DBC template. A longer etching time leads to a slower decrease in the magnetization (in the interval 90s < t_{etch} <120 s), demonstrating that the removal of the upper magnetic layer is almost complete, in agreement with the corresponding SEM image in which nanodots are at this point only partially interconnected. At the etching time necessary to form isolated nanodots (t_{etch} = 150 s) the saturation magnetization is observed to remain practically constant.

In addition, as long as the top layer is not completely removed, the coercivity is seen to decrease as well, whereas full dot separation is marked by a sudden increase in H_C (see Figure 2d) at t_{etch} = 150 s. This result is compatible with reports in literature showing an increment in

the coercivity upon nanostructuring magnetic materials, due to possible shape anisotropies induced by magnetostatic interactions [Kun-Hua Tu, TibertoASS,]. In addition, the coercivity values observed in the reference continuous thin films deposited on the Si substrate (dotted line) and on the DBC mask (t_{etch} = 0 s) are observed to be very different. The very high coercivity value in the latter case can be attributed to both the uneven Co film surface with film-thickness variation on vertical walls of the DBC mask and different stresses arising from the underlying substrate [Albrecht].

Room-temperature magnetic properties of nanodot arrays

Room-temperature hysteresis loops of continuous $Ni_{80}Fe_{20}$ and Co thin films (10 and 13 nm thick respectively) deposited on a flat Si substrate are considered as a reference to study the magnetization reversal process occurring in the magnetic layer deposited onto the DBC mask and in the nanodot array having the same nominal thickness.

Both reference samples display a soft magnetic behaviour, with a slightly larger coercivity for Co, as it can be observed by comparing the hysteresis curves (black line) shown in Figure 3 ($Ni_{80}Fe_{20}$, panel (a) and Co, panel (d)).

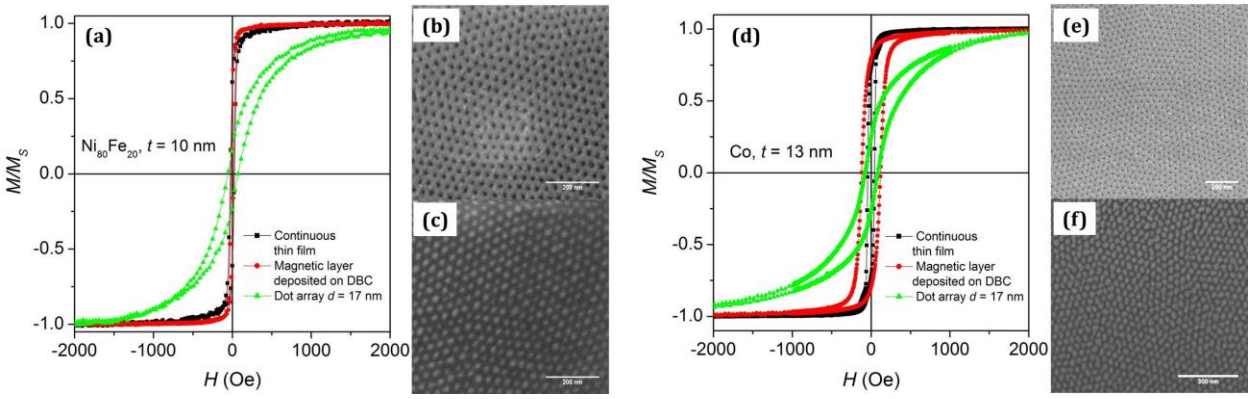

Figure 3. Room temperature hysteresis loops ($Ni_{80}Fe_{20}$ in panel (a), Co in panel (d)): continuous thin film deposited on Si substrate (black line), magnetic layer deposited on DBC matrix (red line) and hysteresis loops of dot array (green line). ($Ni_{80}Fe_{20}$ in panel (b), Co in panel (e)) SEM image of layer deposited on DBC; ($Ni_{80}Fe_{20}$ in panel (a), Co in panel (d)) SEM image of final magnetic nanodot array.

Deposition of the magnetic thin film on top of the DBC mask (SEM images in Figures 3b and 3e) leads to almost unchanged magnetic properties for $Ni_{80}Fe_{20}$, whereas, as previously pointed out, a significant increase in coercivity is observed for Co (red curves in Figures 3a and 3d); this is ascribed to the intrinsically higher magnetocrystalline anisotropy of Co with respect to $Ni_{80}Fe_{20}$. When the top layer is completely removed and the isolated dot arrays are obtained (SEM images in Figures 3c and 3f), both materials display a much slower approach to saturation, marked by a lower susceptibility (green curve in Figures 3a and 3d). As expected, the Co nanodots show larger H_C values with respect to $Ni_{80}Fe_{20}$ ones.

In order to investigate the possible effect of magnetic anisotropy induced during sputtering deposition of Co sample, room-temperature hysteresis loops of the Co nanodots were measured with the magnetic field applied both in-plane and along the out-of-plane direction (normal to the substrate). The two curves normalized to saturation magnetization are reported in Figure 4. As it can be observed, the squareness of in-plane hysteresis loop is slightly higher than the one of out-of-plane loop, indicating a slight preference of the anisotropy easy axis to lie close to the sample plane. This configuration is in agreement with the XRD results performed on a Co thin film sputtered with deposition parameters identical to those used to fabricate the nanodot array having a film thickness of ~ 500 nm in order to gain signal-to-noise ratio as high as possible during the

measurement. The obtained XRD pattern (see Figure M1 in the supplemental material) reveals a dominant hcp phase (hence the experimentally observed magnetic anisotropy) characterized by intense reflection peaks, and a minor fcc phase indicated by lower reflection peaks. According to the magnetic measurements, the hcp crystallites are grown with randomly oriented c-axes with a slight prevalence of in-plane orientation, which together determines together with shape anisotropy the behaviour observed in Figure 4. It is indeed known that Co can exhibit different anisotropy structures, such as hexagonal close-packed (hcp), face-centered cubic (fcc), mixture of fcc-hcp and ε phase, depending on the employed processing techniques [Walia, Matveev] therefore supporting our data.

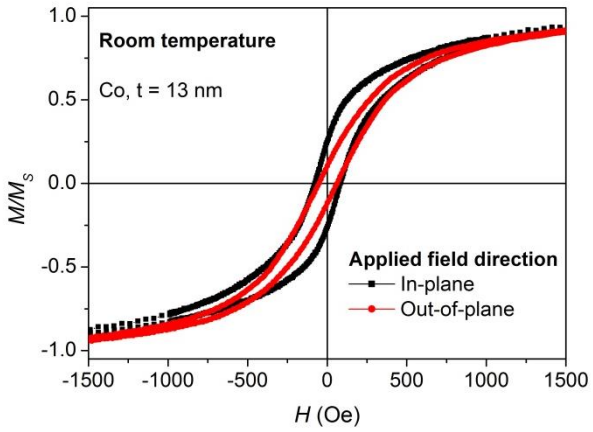

Figure 4. Room temperature hysteresis loops of Co dot array applying the magnetic field in-plane (black curve) and along out-of-plane direction (red curve).

In order to more deeply elucidate the role of magnetocrystalline anisotropy and magnetostatic interactions in the magnetisation reversal process of these close-packed dot arrays, micromagnetic simulations have been performed and will be discussed later.

Magnetization reversal process in Co nanodot array at low-temperatures

The temperature dependence of the magnetization reversal exhibits different features in the dot arrays depending on the chosen magnetic material. To this aim, hysteresis loops have been measured as a function of temperature in different cooling conditions in order to reveal the presence of possible antiferromagnetic native oxide layers magnetically coupled with the ferromagnetic material constituting the nanodots [Nogues]. The hysteresis loops measured with temperature T ranging in the interval 5-300 K and taken with the sample cooled to 5 K from room-temperature under zero applied magnetic field are shown in Figure 5. As expected, Co nanodots are characterized by a regular increase in H_C when reducing temperature (see also Fig. 8c in micromagnetic simulation section), without major variations in the loop shape, suggesting that the overall magnetization reversal process remains unchanged with only a slight increase in magnetic anisotropy and interaction energy due to the expected increase in M_S on decreasing temperature.

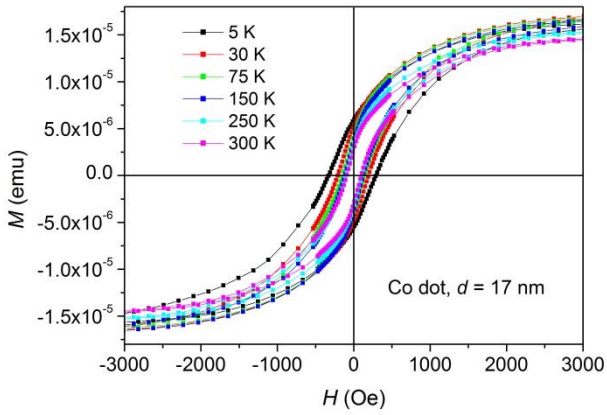

Figure 5. Hysteresis loops of Co dot arrays measured at selected temperatures, after cooling the sample from 300 to 5 K under zero applied magnetic field.

However, an exchange bias effect has been identified by acquiring the hysteresis loops after cooling the sample from room-temperature to 5 K under an applied magnetic field of 10 kOe. The curves are reported in Figure 6a, where a typical loop displacement along the field axis is observed for the hysteresis loops taken at lower temperature. This result confirms the presence of an exchange bias effect due to a Co-oxide native layer on top of the Co nanodots. Such a displacement, measured by the exchange bias field H_{eb}, is experimentally seen to be reduced with increasing temperature, as shown in Figure 6b. The observed effect disappears at temperatures higher than 100 K. This critical value usually corresponds to the Néel temperature (T_N) below which an antiferromagnetic order appears in the Co-oxide layer. In nanostructured Co oxides, T_N has been measured in the interval 70-100 K [Nogues2, Amobrose, VanDerZang], in good agreement with the presented results.

Low-temperature hysteresis loops have been measured also for $Ni_{80}Fe_{20}$ nanodot arrays, however, they do not reveal any exchange bias effect coming from the possible presence of a Ni-oxide layer natively developed on top of the $Ni_{80}Fe_{20}$ dots (see Figure M2 in the supplemental material), as its very weak intensity [Fulcomer] is below the detection limit allowed by our measurement techniques.

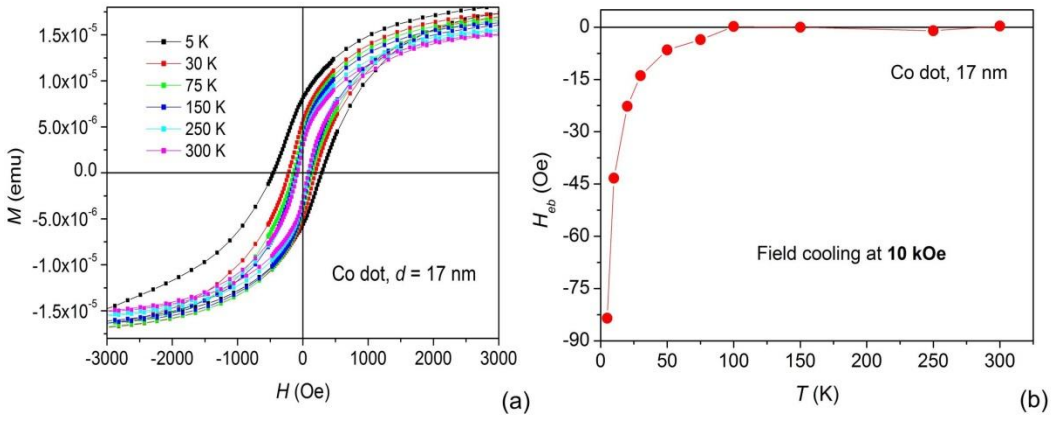

Figure 6. (a) Hysteresis loops of Co nanodot arrays at selected temperatures after a field-cooling at 10 kOe from room-temperature up to 5 K; (b) temperature evolution of exchange bias field of curves in (a).

Micromagnetic simulations

The aim of the micromagnetic modelling analysis is to support the interpretation of experimental results, investigating the impact on magnetization reversal process of possible dipole-dipole interactions among dots, magnetocrystalline anisotropy dispersion and temperature. The attention is focused on the Co dot array.

The fabrication process here adopted contributes to the formation of a complex system having a probable stochastic distribution of anisotropy features among dots, confirmed by the room-temperature hysteresis loops shown in Figure 4, with possible presence of both hcp and fcc structures and interface exchange coupling between the dot magnetic core and the surface Co oxide layer [Iglesias]. To reduce complexity, the dot array will be modelled as a collection of magnetic nanoparticles with random distribution of easy axes, assuming a uniaxial anisotropy for all the dots. This hypothesis will support us in understanding the role of the stochastic character of anisotropy on the hysteresis loop shape, above dipole-dipole interactions and independently of the actual anisotropy structure. Moreover, due to the native origin of the surface Co oxide layer, whose physical properties and thickness cannot be controlled during the fabrication process and thus parameterized, we neglect interface exchange coupling and exchange bias effects in the modeling, referring only to zero-field-cooled measurements.

To investigate the possible contribution of dipole-dipole interactions among dots, the dot array is first simulated as a system with long-range hexagonal order, composed of equal and

periodically distributed dots with a diameter of 17 nm, a thickness of 13 nm and an interdot distance of 35 nm (centre-to-centre), neglecting temperature effects. The saturation magnetization is fixed to 1400 kA/m and the exchange constant to 30 pJ/m (bulk values for cobalt) [Pousthomis], while the magnetocrystalline anisotropy is varied up to 500 kJ/m^3, assuming a main in-plane orientation of the easy axis (in agreement with the comparison between experimental in-plane and out-of-plane hysteresis loops in Figure 4). The simulation results (not shown) have demonstrated that, independently of magnetocrystalline anisotropy, dipolar interactions are very weak for such dot arrangement, with a negligible variation in coercive field and remanent magnetization for the in-plane hysteresis loops with respect to the case of single dot. These outcomes are in agreement with the conclusions reported in [Chun-Hao Lin] for $Ni_{80}Fe_{20}$ dot arrays with similar geometrical properties and packing fraction. It has been numerically verified that the periodically ordered structure does not exhibit a cooperative reversal of the magnetization also when increasing the dot diameter up to 20 nm, value close to the maximum extreme of the dispersion curve of the measured diameters (reported in Figure 1f). Finally, with long-range hexagonal order and constant physical parameters the system is characterized by coherent reversal with synchronous rotation of the magnetization; each dot behaves as a mono-domain particle.

This result also makes unnecessary to model the $Ni_{80}Fe_{20}$ dots, whose lower saturation magnetisation with respect to the Co dots makes dipole-dipole interactions even weaker.

The experimental reversal curves are actually not characterized by a single irreversible jump, but they are spanned over a wide field range. To explain the smoothness of the measured hysteresis loops and eliminate possible finite-size effects, the dot array is more realistically described as a collection of geometric domains with average size of 200 - 300 nm (identifiable in

the SEM image of Figure 1d), introducing dislocation regions with reduced interdot distance. Moreover, magnetocrystalline anisotropy properties are stochastically distributed, assuming a uniaxial anisotropy (hcp), with a random dispersion of easy axis orientation (varied dot-by-dot) and a fixed value of constant anisotropy k_{an} ranging from 50 to 200 kJ/m^3.

Taking into account the comparison between experimental in-plane and out-of-plane hysteresis loops (Figure 4), which reveals a preference for magnetization to be aligned in the film plane (higher remanent magnetization and coercive field), the easy axis orientation is defined by the two spherical coordinates ϕ and θ (see inset of Figure 7c), where azimuthal angle ϕ has a uniform distribution and polar angle θ has a normal distribution with mean 90° and variable standard deviation SD. In order to find the set of parameters leading to the best fit with experimental results and limit overlapping temperature effects, we first focus on the numerical reconstruction of the hysteresis loop measured at 5 K. The corresponding variation of coercive field H_C and remanent magnetization M_R as a function of k_{an} for SD = 40° is shown in Figure 7a. The increase in anisotropy constant leads to an initial rapid increment of M_R and a pronounced variation in H_C at high values of k_{an}. Figure 7b illustrates the dependence of H_C and M_R on standard deviation for k_{an} = 110 kJ/m^3: the rise in SD produces a strong reduction in magnetic susceptibility leading to a smooth reversal of the magnetization, as observed experimentally. Finally, a uniaxial anisotropy of 110 kJ/m^3 and a standard deviation of 40° provide a good reconstruction of the hysteresis loops measured at low temperature, in terms of H_C, M_R and magnetic susceptibility (see Figure 7c). The analysis of magnetization configurations at different equilibrium states (Figure 7d) reveals that the switching starts at the dislocation regions, where interdot interactions are stronger, and in correspondence of the dots whose easy axis is orthogonal to the applied field, where the contribution from magnetocrystalline anisotropy is higher. This could explain the

initial gradual decay of magnetization from saturation observed in the experimental loops. Then, the reversal proceeds in the regions internal to the geometric domains and in the dots with easy axis parallel to the applied field. The magnetization rotation concludes at the dislocation interfaces, where magnetization configuration remains frozen during the intermediate field interval of the loop, and in the dots whose easy axis is orthogonal to the applied field, characterized by a slower switching. This could provide an interpretation of the final gradual decay of magnetization towards opposite saturation observed in the measured loops. Finally, each dot practically behaves like a single-domain particle.

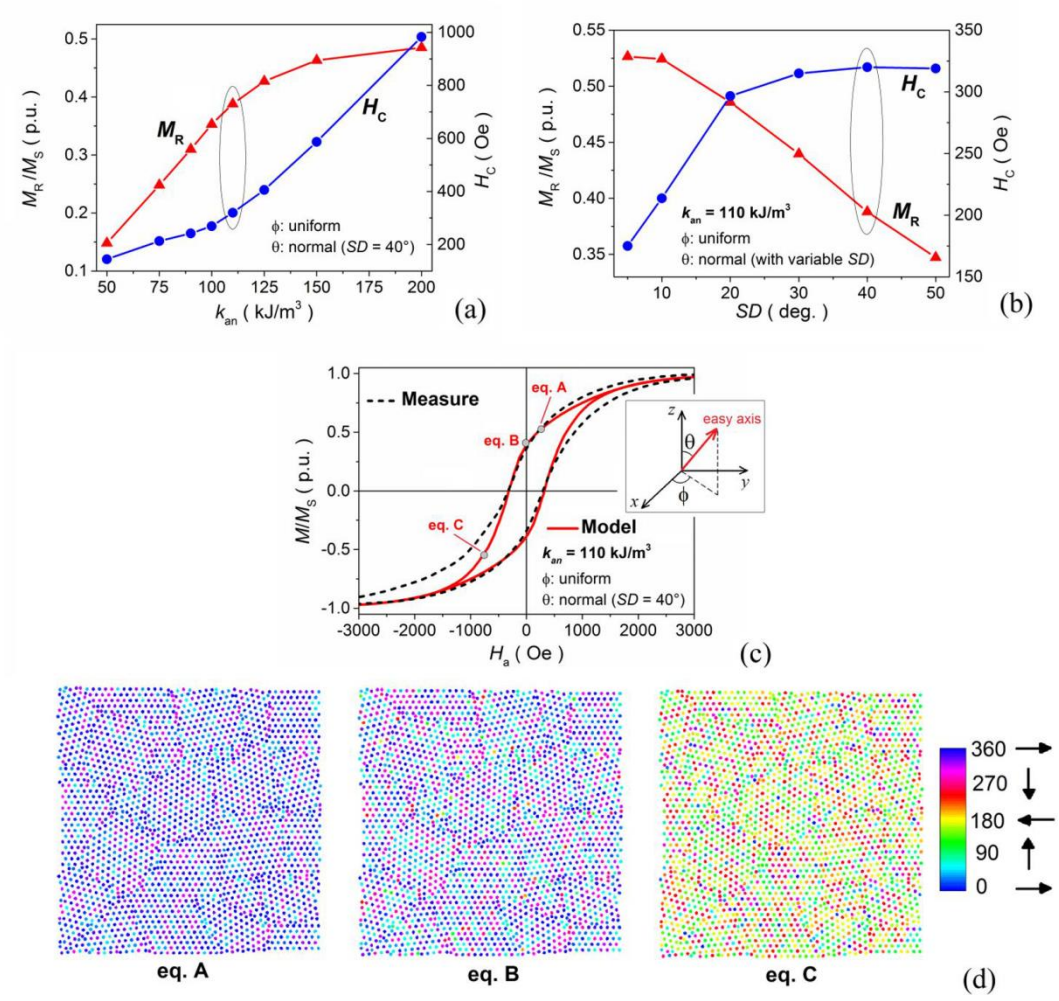

Figure 7. Simulation results obtained for a temperature of 5 K, considering a random distribution of easy axis orientation, where angle ϕ has a uniform distribution and θ has a normal distribution with mean 90˚ and standard deviation SD. The reference system is depicted in the inset of (c), where the *xy*-plane corresponds to the sample plane. (a) Calculated coercive field H_C and remanent magnetization M_R as a function of magnetocrystalline anisotropy constant k_{an} for SD = 40˚. (b) Calculated values of H_C and M_R versus SD for k_{an} = 110 kJ/m^3. The circles indicate the parameters leading to the best agreement with measurements. (c) Comparison of the experimental hysteresis loop to the one calculated with the optimal parameters (k_{an} = 110 kJ/m^3 and SD = 40˚). (d) Magnetization spatial distributions computed at the equilibrium points marked along the simulated curve in (c). The colour scale, on the right, identifies the in-plane magnetization angle (in degrees) with respect to *x*-axis.

The same physical parameters lead to a good reconstruction of the experimental results also for higher temperatures, as demonstrated by Figures 8a and 8b, which report the loops calculated and measured for T = 5 K, 20 K and 300 K, respectively. Also micromagnetic simulations confirm a compression of the hysteresis cycles at the increase in temperature. The estimated influence of temperature on H_C and M_R is shown in Figures 8c and 8d, where the uncertainty bars take into account a variation of ±10 kJ/m^3 in k_{an} and of 10˚ in the standard deviation of the normal distribution of θ, considering different stochastic distributions of easy axis orientation. The simulation results are compared to the experimental ones derived from zero-field-cooled hysteresis loops, from which the coercive field and the remanent magnetization have been estimated by averaging the values obtained in the two loop branches. For both simulation and experimental data, which are in very good agreement, the effects of thermal agitation are more

evident in the initial interval of variation of temperature (up to <50 K), where the random distribution of thermal field competes with the stochastic distribution of magnetocrystalline anisotropy fields. Then, temperature effects become dominant, leading to a more chaotic switching, where the collective reversal observed at the dislocations regions is strongly reduced and each dot behaves independently, with less pronounced single-domain features. Anyway, the system maintains a ferromagnetic behavior without transition to superparamagnetism. The modification of the magnetization configuration caused by the temperature increase is well illustrated in Figure 8e, which reports the spatial distribution of the magnetization at remanence state calculated for T = 5 K, 20 K and 300 K. In particular, the very low remanent magnetization found at room temperature can be explained by the obtained chaotic distribution of the magnetization orientation.

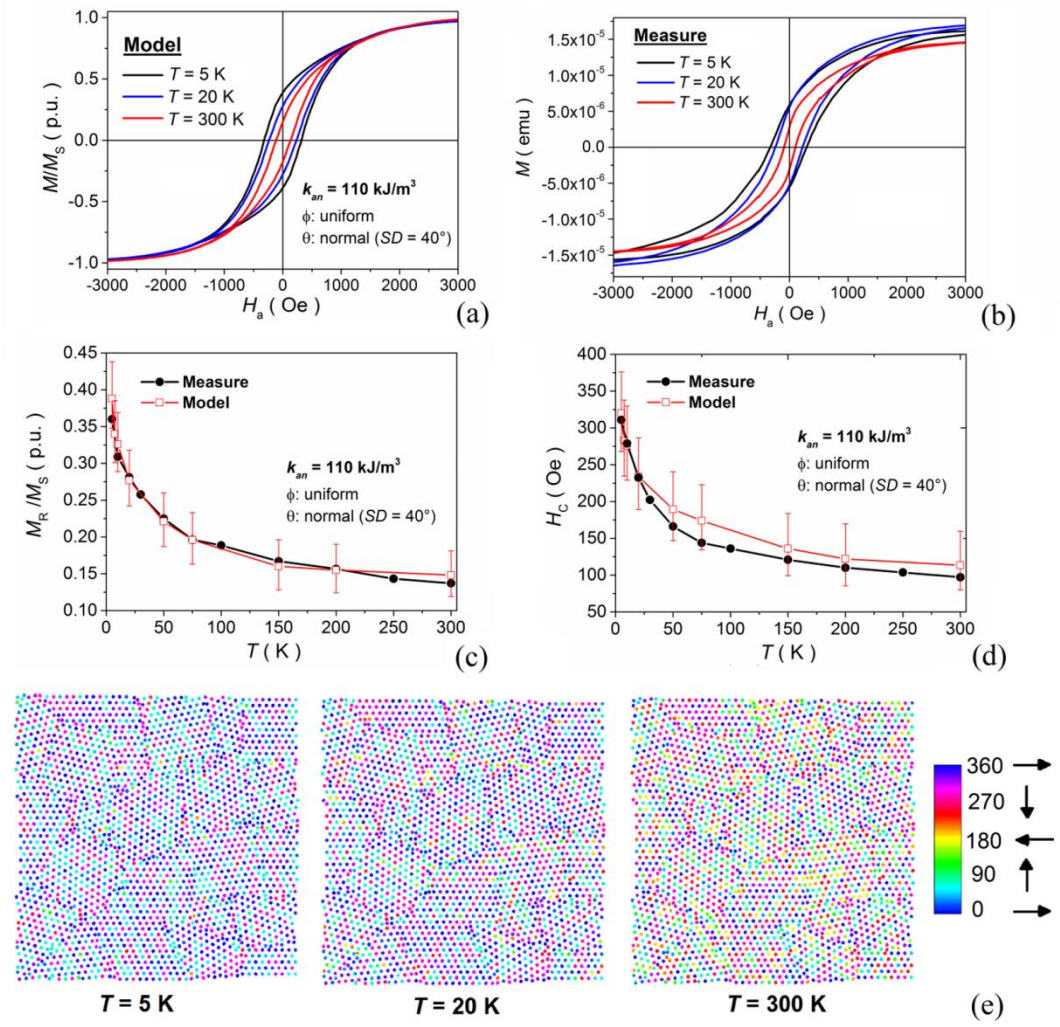

Figure 8. Simulation results obtained as a function of temperature, considering a random distribution of easy axis orientation, where angle ϕ has a uniform distribution and θ has a normal distribution with mean 90˚ and standard deviation SD = 40˚. The anisotropy constant is fixed to 110 kJ/m^3. Calculated (a) and measured (b) hysteresis loops at different temperatures. (c) Remanent magnetization (c) and coercive field (d) versus temperature: comparison between modelling and measurement results. The uncertainty bars reported on the calculated curves take into account a variation of ±10 kJ/m^3 in k_{an} and of 10˚ in the standard deviation of the normal distribution of θ. (e) Magnetization spatial distributions calculated at remanence state for

different temperatures. The colour scale, on the right, identifies the in-plane magnetization angle (in degrees) with respect to *x*-axis.

CONCLUSIONS

In this work, a fine-tuned process based on the combination of block copolymer templating, sputtering deposition, and sputter-etching at a glancing angle of 45° has been successfully exploited to pattern $Ni_{80}Fe_{20}$ and Co thin films into a highly ordered large-area nanodot arrays having 17 nm diameter. In particular, the 45°-sputter-etching step of fabrication process comes out as an effective, powerful method to nanostructure magnetic thin films overcoming limitations proper of conventional lithographic techniques.

To summarize, the magnetic properties of Co nanodot arrays are characterized by a slow approach to magnetization saturation also marked by an almost linear reduction of M_R/M_S value as a function of the 45°-sputter-etching time. The formation of isolated magnetic nanodots is evidenced by a sudden increase in H_C. Co nanodot arrays turn out to exhibit a slight preferential magnetic anisotropy orientation along the plane of the sample; moreover, the development of a native antiferromagnetic Co-oxide layer covering nanodots is responsible for an exchange bias effect occurring below Neél temperature.

Micromagnetic simulations give a complete picture of the magnetization switching process taking place in nanodot arrays providing an overall reconstruction of the experimental data acquired at all measured temperatures. In particular, the modelling analysis suggests the negligibility of magnetostatic dipolar interactions among nanodots, describing the smooth reversal of the magnetization as a result of competing contributions from thermal field and stochastic distribution of magnetocrystalline anisotropy properties.

METHODS

Substrate neutralization

The P(S-*r*-MMA) random copolymer (RCP) with styrene fraction XS = 0.618, Molar Mass M_n = 1.7 kg·mol^{-1} and *PDI* = 1.19 was previously synthesized as described in ref. [Sparnacci]. A solution with 18 mg of P(S-r-MMA) in 2 ml of toluene was prepared in ultrasonic bath. The -OH terminations of the random copolymer were used to graft the copolymer to the native silicon oxide layer. The P(S-*r*-MMA) solution was spun for 30 seconds at 3000 rpm. In order to induce the grafting of the RCP onto the substrate, the samples were annealed at high temperature in the rapid thermal processing (RTP) machine at 300 °C for 60 s. The non-anchored chains were subsequently removed with a 300 s sonication bath in toluene, resulting in a ~ 2 nm thick neutral layer.

Block copolymer deposition

The asymmetric PS-b-PMMA DBC having styrene unit fraction of 0.71, M_n = 67.1 kg·mol^{-1} and *PDI* = 1.09 was purchased from Polymer Source Inc. and used without further purification. A solution with PS-*b*-PMMA in toluene was prepared (18 mg in 2 ml) and spin coated on the previously neutralized substrate. The RTP annealing was performed in N_2 atmosphere at 250 °C for 300 s, in order to promote self-organization into hexagonal arrangements of PMMA cylinders in a PS matrix. The domain period of such cylindrical features is L_0 ~ 35 nm while the cylinder diameter is d ~ 17 nm. The formation of the PS nanotemplate was completed by the selective removal of the PMMA, obtained by exposing the samples for 300 s to ultraviolet radiation (5 mW·cm^{-2}, λ = 253.7 nm). This step allowed the degradation of the PMMA that can be later removed by an immersion of the sample in an acetic acid bath and a subsequent rinsing in deionized water. Due to the small thickness of the RCP layer, a short oxygen plasma treatment of

30 s was sufficient to remove the RCP at the bottom of the pores. The short duration of the plasma treatment prevents the excessive crosslinking of the PS matrix, facilitating as consequence the lift-off process in toluene.

Magnetic material deposition and characterisation

RF-sputtering deposition technique was used to deposit magnetic materials ($Ni_{80}Fe_{20}$ or Co) in thin film form (thickness 10 and 13 nm, respectively). The deposits onto the BCP template resulted in magnetic dot arrays obtained following the process described in Section "Results and Discussion". Those sputtered onto Si substrates, instead, served as continuous magnetic reference materials. The deposition parameters were kept the same for all depositions: base pressure of the sputtering was set at 1×10^{-7} mbar, power at 50 W and Ar gas pressure at 1×10^{-2} mbar. The deposition time was calculated from the deposition rate of $Ni_{80}Fe_{20}$ and Co materials (1.3 Å/s) in order to obtain the desired thickness.

Ar^+ sputter-etching technique was used to remove the magnetic materials on top of the BCP matrix in order to obtain dot arrays. This step is performed at a glancing angle of 45° with respect to the magnetic film plane, as discussed in Section "Results and Discussion". The etching parameters were kept the same for all samples: power was set at 100 W and process pressure at 1×10^{-2} mbar. The time of sputter-etching process (t_{etch}) was incremented gradually (step-by-step) in order to investigate the effect of the removal of magnetic material on the magnetic properties until obtaining the final magnetic dot arrays.

FEI Inspect-F™ Field Emission Gun scanning electron microscope (FEG-SEM) was used to investigate the morphology of the BCP template and of all the magnetic samples. A software analysis of SEM images of dot arrays enables to calculate the size distribution of the dots.

Room-temperature magnetic characterization was performed by means of a high-sensitive alternating gradient field magnetometer (AGFM) operating in the field range –18 kOe < H < 18 kOe. The isothermal hysteresis loops at cryogenic temperatures were measured on final nanodot arrays by a SQUID magnetometer operating in the field range –70 kOe < H < 70 kOe and in the temperature interval 5 – 300 K.

Micromagnetic simulation

The experimental results have been interpreted by means of micromagnetic simulations, performed with a micromagnetic solver designed to run on graphic processing unit cards [Bottauscio]. The code adopts a time integration scheme based on Cayley transform and Heun algorithm for the update of the magnetization in the Landau-Lifshitz-Gilbert (LLG) equation and the efficient calculation of static hysteresis loops [Manzin, Manzin2]. The exchange field is computed with a finite difference method able to handle non-structured meshes, thus enabling a more accurate description of curvilinear boundaries [Bottauscio2]. Temperature effects are simulated via a Langevin approach [Manzin3, Martínez], adding a thermal field to the effective field in the LLG equation. The thermal field $\mathbf{H}_{\mathrm{th}}(\mathbf{r},t)$ is assumed to be a Gaussian random process expressed as

$$\mathbf{H}_{\mathrm{th}}\left(\mathbf{r},t\right)=\boldsymbol{\eta}_{\mathrm{th}}\left(\mathbf{r},t\right)\sqrt{\frac{2\alpha k_{\mathrm{B}}T}{\gamma\mu_0 M_{\mathrm{S}}\Delta s^3\Delta t}}$$

where $\boldsymbol{\eta}_{\mathrm{th}}(\mathbf{r},t)$ is a stochastic vector whose components are Gaussian random numbers, uncorrelated in space and time, with zero mean value and dispersion 1, α is the damping coefficient, T is the absolute temperature, k_B is the Boltzmann constant, γ is the gyromagnetic ratio, M_S is the saturation magnetization, Δs is the average length of the spatial discretization, and Δt is the time step used in the numerical algorithm.

ACKNOWLEDGMENT

The authors would like to thank E. S. Olivetti for providing XRD measurement and data analysis. Part of this work has been performed at Nanofacility INRiM, a laboratory supported by Compagnia di San Paolo Foundation.

REFERENCES

[Nalwa] Nalwa, H. S. Magnetic nanostructures, American Scientific Publishers, USA, 2002

[Yang] Yang, E.; Liu, Z.; Arora, H.; Wu, T.; Ayanoor-Vitikkate, V.; Spoddig, D.; Bedau, D.; Grobis, M.; Gurney, B. A.; Albrecht, T. R.; Terris, B. Template-Assisted Direct Growth of 1 Td/in^2 Bit Patterned Media, *Nano Lett.* **2016**, *16*, 4726-4730.

[Bai] Bai, W.; Ross, C. A. Functional nanostructured materials based on self-assembly of block copolymers, *MRS Bulletin*, **2016**, *41*, 100 – 107.

[Owens] Owens, F. J. Fabrication of Magnetic Nanostructures in *Physics of Magnetic Nanostructures* Owens, F. J., Ed.; John Wiley & Sons, Hoboken: New Jersey, 2015.

[Adeyeye] Adeyeye, A. O.; Singh, N. Large area patterned magnetic nanostructures, *J. Phys. D: Appl. Phys*. **2008**, *41*, 153001

[Tiberto] Tiberto, P; Boarino, L.; Celegato, F; Barrera, G.; Coisson, M.; De Leo, N.; Vinai, F. Large-area patterned magnetic nanostructures by self-assembling of polystyrene nanospheres. *MRS Proceedings,* **2012**, 1411

[Goiriena-Goikoetxea] Goiriena-Goikoetxea, M.; García-Arribas, A.; Rouco, M.; Svalov, A. V.; Barandiaran, J. M. High-yield fabrication of 60 nm Permalloy nanodiscs in well-defined magnetic vortex state for biomedical applications, *Nanotechnology,* **2016**, *27*, 10pp.

[Gross] Gross, L.; Schlittler, R. R.; Meyer, G.; Allenspach, R. Magnetologic devices fabricated by nanostencil lithography, *Nanotechnology*, **2010**, *21*, 325301 (6pp).

[Ruiz] Ruiz, R.; Dobisz, E.; Albrecht, T. R. Rectangular Patterns Using Block Copolymer Directed Assembly for High Bit Aspect Ratio Patterned Media, *ACS Nano*, **2011**, *5(1)*, 79-84.

[Olayo-Valles] Olayo-Valles, R.; Lund, M. S.; Leighton, C.; Hillmyer, M. A. Large area nanolithographic templates by selective etching of chemically stained block copolymer thin films, *J. Mater. Chem.*, **2004**, *14*, 2729 – 2731.

[Shin] Shin, K.; Leach, K. A.; Goldbach, J. T.; Ha Kim, D.; Young Jho, J.; Tuominen, M.; Hawker, C. J.; Russell, T. P. A Simple Route to Metal Nanodots and Nanoporous Metal Films, *Nano Lett.*, **2002**, *2(9)*, 933-936.

[Valbusa] Valbusa, U.; Boragno, C.; Buatier de Mongeot, F. Nanostructuring surfaces by ion sputtering, *J. Phys.: Condens. Matter*, **2002**, *14*, 8153–8175.

[Zhu] Zhu, M.; McMichael, R. D. Effect of interactions on edge property measurements in magnetic multilayers, *J. Appl. Phys.*, **2011**, *109*, 043904.

[Iliexski] Ilievski, F.; Ross, C. A.; Vancso, G. J. Magnetic reversal phenomena of perpendicular magnetic islands fabricated by block copolymer lithography, *J. Appl. Phys.*, **2008**, *103*, 07C520

[ITRS International Technology Roadmap for Semiconductors (ITRS), Emerging Research Materials 2011]

[Baruth] Baruth, A.; Rodwogin, M. D.; Shankar, A.; Erickson, M. J.; Hillmyer, M. A.; Leighton, C. Non-lift-off Block Copolymer Lithography of 25nm Magnetic Nanodot Arrays, *ACS Appl. Mater. Interfaces*, **2011**, 3, 3472–3481.

[Kun-Hua Tu] Tu, K-H.; Bai, W.; Liontos, G.; Ntetsikas, K.; Avgeropoulos, A.; Ross, C. A. Universal pattern transfer methods for metal nanostructures by block copolymer lithography, *Nanotechnology*, **2015**, *26*, 375301 (12pp).

[Hawker] Hawker, C. J.; Russell, T. P. Block Copolymer Lithography: Merging "Bottom-Up" with "Top-Down" Processes, *MRS Bullettin*, **2005**, *30*, 952 – 966.

[Hamley2] Hamley, I. W. Ordering in thin films of block copolymers: Fundamentals to potential applications, *Prog. Polym. Sci.*, **2009**, *34*, 1161–1210.

[Jung] Jung, Y. S., Ross, C. A. Well-Ordered Thin-Film Nanopore Arrays Formed Using a Block-Copolymer Template, *Small*, **2009**, *5(14)*, 1654–1659.

[Tavakkoli] Tavakkoli K. G., A.; Gotrik, K. W.; Hannon, A. F.; Alexander-Katz, A.; Ross, C. A.; Berggren, K. K. Templating Three-Dimensional Self-Assembled Structures in Bilayer Block Copolymer Films, *Science*, **2012**, *336*, 1294-1298.

[Suh] Suh, H. S.; Kim, D. H.; Moni, P.; Xiong, S.; Ocola, L. E.; Zaluzec, N. J.; Gleason, K. K.; Nealey, P. F. Sub-10-nm patterning via directed self-assembly of block copolymer films with a vapour-phase deposited topcoat, *Nat. Nanotechnol.*, **2017**, (9pp)

[Hamley1] Hamley, I. W. Nanostructure fabrication using block copolymers, *Nanotechnology*, **2013**, *14*, R39–R54.

[Perego] Perego, M.; Ferrarese Lupi, F.; Ceresoli, M.; Giammaria, T. J.; Seguini, G.; Enrico, E.; Boarino, L.; Antonioli, D.; Gianotti, V.; Sparnacci, K.; Laus, M. Ordering dynamics in symmetric PS-b-PMMA diblock copolymer thin films during rapid thermal processing, *J. Mater. Chem. C*, **2014**, 2, 6655-6664.

[Ferrarese] Ferrarese Lupi, F.; Giammaria, T. J.; Seguini, G.; Vita, F.; Francescangeli, O.; Sparnacci, K.; Antonioli, D.; Gianotti, V.; Laus, M.; Perego, M. Fine Tuning of Lithographic Masks through Thin Films of PS-b-PMMA with Different Molar Mass by Rapid Thermal Processing, *ACSnano ACS Appl. Mater. Interfaces*, **2014**, *6*, 7180−7188.

[Ferré] Ferré, J. Dynamics of Magnetization Reversal: From Continuous to Patterned Ferromagnetic Films, in *Spin Dynamics in Confined Magnetic Structures* Hillebrands, I, B.; Ounadjela, K.; Eds., Springer, 2001.

[Chun-Hao Lin] Lin, C-H.; Polisetty, S.; O'Brien, L.; Baruth, A.; Hillmyer, M. A.; Leighton, C.; Gladfelter, W. L. Size-Tuned ZnO Nanocrucible Arrays for Magnetic Nanodot Synthesis via Atomic Layer Deposition-Assisted Block Polymer Lithography, *ACS Nano*, **2015**, *9(2)*, 1379–1387.

[Skrm2] Woo, S.; Litzius, K.; Krüger, B.; Im, M-Y.; Caretta, L.; Richter, K.; Mann, M.; Krone, A.; Reeve, R. M.; Weigand, M.; Agrawal, P.; Lemesh, I.; Mawass, M.-A.; Fischer, P.; Kläui, M.; Beach, G. S. D. Observation of room-temperature magnetic skyrmions and their current-driven dynamics in ultrathin metallic ferromagnets, *Nature Materials*, **2016,** *15*, 502-507.

[Cheng] Cheng, J. Y.; Ross, C. A.; Thomas, E. L.; Smith, H. I.; Lammertink, R. G. H.; Vancso, G. J. Magnetic Properties of Large-Area Particle Arrays Fabricated Using Block Copolymer Lithography, *IEEE Transactions On Magnetics*, **2002**, *38(5)*, 2541-2543.

[Chen Xu] Xu, C.; Ohno, K.; Ladmiral, V.; Composto, R. J. Dispersion of polymer-grafted magnetic nanoparticles in homopolymers and block copolymers, *Polymer*, **2008**, *49*, 3568-3577.

[Cowburn] Cowburn, R. P.; Adeyeye, A. O.; Welland, M. E. Controlling magnetic ordering in coupled nanomagnet arrays, *New Journal of Physics 1*, **1999**, 16.1–16.9.

[Perego2] Perego, M.; Andreozzi, A.; Vellei, A.; Ferrarese, F.; Seguini, G. Collective behavior of block copolymer thin films within periodic topographical structures, *Nanotechnology*, **2013**, *24*, 245301 (8pp).

[TibertoASS] Tiberto, P.; Boarino, L.; Celegato, F.; Barrera, G.; De Leo, N.; Coisson, M.; Vinai, F.; Allia, P. Arrays of nanostructured antidot in $Ni_{80}Fe_{20}$ magnetic thin films by photolithography of polystyrene nanospheres, *Applied Surface Science*, **2012**, 259, 44– 48.

[Albrecht] Albrecht, M.; Hu, G.; Guhr, I. L.; Ulbrich, T. C.; Boneberg, J.; Leiderer, P.; Schatz, G. Magnetic multilayer on nanospheres, *Nature Mater.*, **2005**, *4*, 203-206.

[Matveev] Matveev, V. V.; Baranov, D. A.; Yurkov, G. Y.; Akatiev, N. G.; Dotsenko, I. P.; Gubin, S. P. Cobalt nanoparticles with preferential hcp structure: A confirmation by X-ray diffraction and NMR, *Chemical Physics Letters*, **2006**, *422*, 402–405.

[Walia] Walia, R.; Pivin, J. C.; Chawla, A. K.; Jayaganthan, R.; Chandra, R. Structural and magnetic properties of sputter deposited cobalt–silica nanocomposite thin films, *Journal of Alloys and Compounds*, **2011**, *509*, L103–L108.

[Nogues] Nogues, J.; Schuller, I. K. Exchange Bias, *J. Mag. Mag. Mater.*, **1999**, *192*, 203-232

[Nogues2] Nogués, J.; Sort, J.; Langlais, V.; Skumryev, V.; Suriñach, S.; Muñoz, J.S.; Baró, M.D. Exchange bias in nanostructures, *Physics Reports*, **2005**, *422*, 65 – 117

[Ambrose] Ambrose, T. ; Chien, C. L. Finite-Size Effects and Uncompensated Magnetization in Thin Antiferromagnetic CoO Layers, *Phys, Rev. Lett.*, **1196**, *76(10)*, 1743-1746.

[VanDerZang] van der Zaag, P. J.; Ijiri, Y.; Borchers, J. A.; Feiner, L. F.; Wolf, R. M.; Gaines, J. M.; Erwin, R.W.; Verheijen, M. A. Difference between Blocking and Néel Temperatures in the Exchange Biased Fe_3O_4/CoO System, *Phys. Rev. Lett.*, **2000**, *84(26)*, 6102-6105.

[Fulcomer] Fulcomer, E.; Charap, H.; Temperature and frequency dependence of exchange anisotropy effects in oxidized NiFe films, *J. Appl. Phys.*, **1972**, *43(10)*, 4184-4189.

[Iglesias] Iglesias, Ò.; Labarta, A.; Batlle, X. Exchange bias phenomenology and models of core/shell nanoparticles, *J. Nanosci. Nanotechnol.*, **2008**, *8*, 2761–2780.

[Pousthomis] Pousthomis, M.; Anagnostopoulou, E.; Panagiotopoulos, I.; Boubekri, R.; Fang, W.; Ott, F.; Atmane, K. A.; Piquemal, J.-Y.; Lacroix, L.-M.; Viau, G. Localized magnetization reversal processes in nanorods with different aspect ratios, *Nano Research*, **2015**, 11pp.

[Sparnacci] Sparnacci, K.; Antonioli, D.; Gianotti, V.; Laus, M.; Ferrarese Lupi, F.; Giammaria, T. J.; Seguini, G.; Perego, M. Ultrathin Random Copolymer-Grafted Layers for Block Copolymer Self-Assembly, *ACS Appl. Mater. Interfaces*, **2015**, *7(20)*, 10944–10951.

[Bottauscio] Bottauscio, O.; Manzin, A. Parallelized micromagnetic solver for the efficient simulation of large patterned magnetic nanostructures, *J. Appl. Phys.,* **2014**, *115*, 17D122.

[Manzin] Manzin A.; Bottauscio, O. Connections between numerical behavior and physical parameters in the micromagnetic computation of static hysteresis loops, *J. Appl. Phys.*, **2010**, *108*, 093917.

[Manzin2] Manzin A.; Bottauscio, O. A micromagnetic solver for large-scale patterned media based on non-structured meshing, *IEEE Transactions on Magnetics*, **2012**, *48*, 2789-2792.

[Bottauscio2] Bottauscio O.; Manzin, A. Spatial reconstruction of exchange field interactions with a finite difference scheme based on unstructured meshes, *IEEE Transactions on Magnetics*, **2012**, *48*, 3250-3253.

[Manzin3] Manzin, A.; Van de Wiele, B.; Bottauscio, O.; Dupré, L.; Olyslager, F.; De Zutter, D. Numerical analysis of the influence of geometry and temperature on switching processes in magnetic nanostrips, *IEEE Transactions on Magnetics*, **2010**, *46*, 243-246.

[Martínez] Martínez, E.; López-Díaz, L.; Torres, L.; García-Cervera, C. J. Minimizing cell size dependence in micromagnetics simulations with thermal noise, *J. Phys. D: Appl. Phys.*, **2007**, *40*, 942–948.